



# Faceted and dendritic morphology change in alloy solidification

P.C. Bollada\*, P.K. Jimack, A.M. Mullis

University of Leeds, United Kingdom

## ARTICLE INFO

### Article history:

Received 1 August 2017

Received in revised form 4 December 2017

Accepted 5 December 2017

Available online 16 December 2017

### Keywords:

Crystal formation

Phase field

Alloy solidification

Non-equilibrium thermodynamics

## ABSTRACT

We present methods and results for the simulation of faceted and dendritic crystal growth. Using a thermodynamically realistic isothermal alloy model for AlSi we demonstrate, in confirmation of experimental observations, a change in morphology from perfectly faceted hexagons at smaller undercooling to dendritic growth at larger undercoolings. We also demonstrate that there exists a cut off temperature which separates the two distinct morphologies, and indeed hybrid morphologies. These results suggest that the mechanism for morphology variation observed experimentally primarily lies in anisotropic surface free energy modelling, which we adopt in preference to kinetic anisotropy.

© 2017 The Authors. Published by Elsevier B.V. This is an open access article under the CC BY license (<http://creativecommons.org/licenses/by/4.0/>).

## 1. Introduction

During solidification close to equilibrium crystal morphologies adopt the Wulff shape, which is itself a reflection of the underlying crystallography. However, at large departures from equilibrium alternate morphologies are often adopted. One manifestation of this is that crystals that are faceted at equilibrium become progressively less faceted and more dendritic in character with increasing growth velocity. Such a range of transitions was elegantly demonstrated by [1] in respect of Si crystals growing from an Al-Si melt solidified on a chill plate, with the transition also having been widely studied in the semiconductors Si [2,3] and Ge [4,5] together with Si-Ge [1] mixtures. Where measurements have been made of the growth velocity [2,5] the transition from faceted to dendritic growth is usually accompanied by an abrupt increase in growth velocity. In recent experimental work [6] found, in  $\text{Cu}_6\text{Sn}_5$ , there to be a change from faceted rods to non-faceted dendrites as the cooling rate was increased.

To date the modelling of two-phase crystal growth has concentrated on either continuous dendritic morphology or faceted growth. Here we present an approach to modelling facets that also allows for a transition to a continuous (dendritic) morphology under large departures from equilibrium and also accommodates the intermediate morphology of faceted dendrites. Hence, we clarify that the main mechanism for morphology change is in fact undercooling (and not cooling rate).

In [1] solidified crystals on a chill plate are seen to exhibit a range of morphologies. The observation is that of faceted crystals forming from smooth nuclei at small undercoolings, near equilibrium, giving polyhedra. At greater undercooling dendritic instability may set in before subsequently forming facets thereby giving rise to a faceted dendritic morphology. Most phase field simulations designed to simulate faceted growth only exhibit facets, [8,10–14,18,19], and, of course, the vast majority of phase-field simulations do not show facets at all.

The modelling of facets in phase field is done via a specification of the surface energy, the mobility, or both. We focus on surface energy anisotropy modelling. The link between the surface energy anisotropy and the resulting morphology is discussed in [7]. Crucially, though, the predicted morphology is only strictly valid at small undercooling. The question to be asked is therefore: what happens to the morphology of the solid as the undercooling in increased? In [9] dendritic growth is observed for a pure metal with four-fold symmetry, where, at the tip of the dendrite arms, facets are exhibited. The difference between this and the present work is that we simulate a given specific alloy (AlSi) using a full thermodynamic description, and explore the dependency of morphology on undercooling. We demonstrate that, indeed, facets occur at small undercooling and dendritic growth patterns are observed at high undercooling, with a continuous range of morphologies in between. We model AlSi in two dimensions, with the specification that hexagonal facets are to be formed at near equilibrium. A comprehensive overview of modelling approaches is given in [17], where in general anisotropy can be modelled in both the interface and/or in the mobility. If the anisotropy is in the mobility only, the effect vanishes (within phase-field at least)

\* Corresponding author.

E-mail address: [p.c.bollada@leeds.ac.uk](mailto:p.c.bollada@leeds.ac.uk) (P.C. Bollada).

as  $V \rightarrow 0$ , so this does not give faceted growth during equilibrium solidification. As a minimum, using a capillary anisotropy is therefore a computational expedient to simulating the faceted to continuous growth transition.

We apply the computational techniques detailed in [20].

## 2. Facets and anisotropy modelling

Within the phase field model the surface features are modelled using the gradients of the phase,  $\nabla\phi$  (the detailed phase model is given in Section 3).

Much of the literature concerns 4-fold symmetric growth, so we use this to illustrate the modelling. A 4-fold anisotropy used in the literature to generate 4-fold dendrites is given by

$$A = \frac{1}{2} \delta^2 [1 + \epsilon \cos(4\theta)]^2 \nabla\phi \cdot \nabla\phi. \quad (1)$$

which is controlled by a parameter,  $\epsilon$ , which when zero give isotropic growth. This can also be written

$$A = \frac{1}{2} \delta^2 \gamma^2 \quad (2)$$

where, in general, for  $m$ -fold symmetry

$$\gamma = [1 + \epsilon \cos(m\theta)] |\nabla\phi|. \quad (3)$$

$\gamma$  is also a function of the surface normal in the following sense

$$\begin{bmatrix} \cos \theta \\ \sin \theta \end{bmatrix} = \frac{\nabla\phi}{|\nabla\phi|} \equiv \mathbf{n}. \quad (4)$$

and has the property  $\gamma(\alpha\mathbf{n}) = \alpha\gamma(\mathbf{n})^1$  for any function,  $\alpha$ . It is also convenient to consider the function,  $\eta$ , related to  $\gamma$  by  $\gamma = \eta|\nabla\phi|$ . This function has the property  $\eta(\alpha\mathbf{n}) = \eta(\mathbf{n})$ . Fig. 1 plots  $\eta$  as a function of  $\theta$  in a polar plot, where we see that the circle deforms with increasing  $\epsilon$  to a point where there are concave regions, here illustrated for  $\epsilon = 0.1$ . Setting the locus of the curve

$$\mathbf{x}(\theta) = \eta(\theta) [\cos \theta, \sin \theta]^T, \quad (5)$$

a concave region occurs if

$$\frac{\partial}{\partial\theta} |\mathbf{x}'(\theta)| = 0 \quad (6)$$

for some  $\theta$ , which gives the condition to avoid concavity as  $\eta''(\theta) + \eta(\theta) > 0$ . For the case just considered this implies  $\epsilon < 1/15$  to avoid concavity, and in general  $\epsilon < 1/(m^2 - 1)$  for  $m$ -fold symmetry. Another, more direct, way of illustrating the anisotropy function,  $\gamma$ , is by way of a Frank diagram (or shape). Here we choose a contour of  $\gamma$  in the space  $[\phi_x, \phi_y]$ , see Fig. 2. The problem of concavity in the anisotropy function is that the resulting crystal shape can develop discontinuities in these regions, which in turn presents numerical difficulties.

By writing

$$\gamma_x \equiv \frac{\partial\gamma}{\partial\phi_x}, \quad \gamma_y \equiv \frac{\partial\gamma}{\partial\phi_y}, \quad (7)$$

both of which are functions of  $\phi_x$  and  $\phi_y$ , a 2D space curve,  $W(t)$ , can be produced by setting  $[\phi_x = \cos(t), \phi_y = \sin(t)]$  in functions  $\gamma_x$  and  $\gamma_y$  to give  $W(t) = [\gamma_x(t), \gamma_y(t)]$ . This is shown in Fig. 3 for the four-fold symmetry case, where cusps, known as ‘‘ears’’, form on the  $\epsilon = 0.1 > 1/15$  curve, which correspond to the concavity in the Frank diagram (Fig. 2). Formally the Wulff shape is the shape enclosed by  $W(t)$  (without the ears). The 4-fold anisotropy discussed so far cannot produce facets, rather, as the parameter  $\epsilon$  increases a sharp corner is produced on an otherwise rounded

**Polar plot**

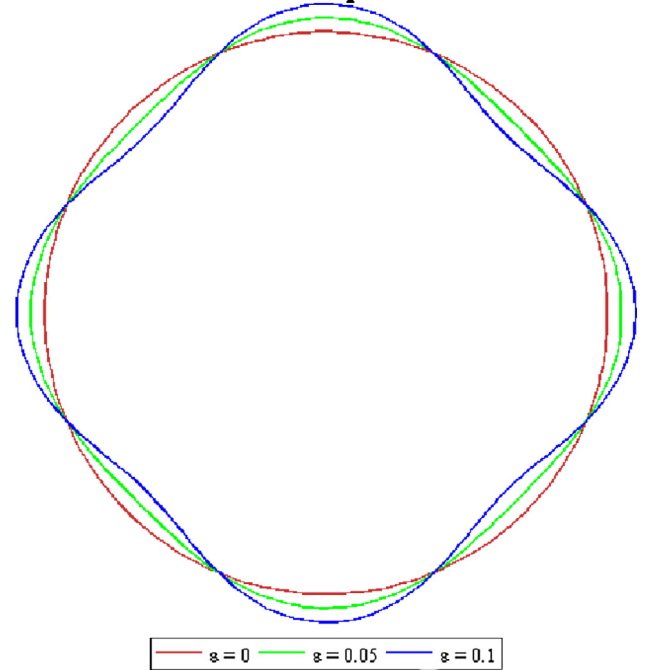


**Fig. 1.** Polar plot of the function,  $\eta = 1 + \epsilon \cos(4\theta)$ , with anisotropy varying from zero (isotropic – red) to extreme anisotropy (blue). The blue curve exhibits concave regions. (For interpretation of the references to color in this figure legend, the reader is referred to the web version of this article.)

**Frank diagram**

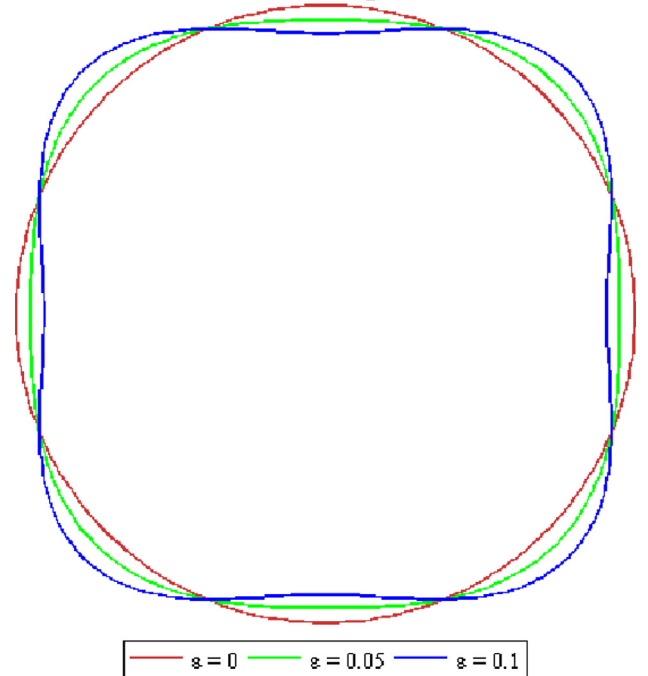


**Fig. 2.** The Frank diagram of the 4-fold anisotropy function is a contour of  $\gamma$  in the space  $[\phi_x, \phi_y]$ . Each contour is identical in shape and is conical for  $\epsilon = 0$ .

shape (a bulging square). So we seek other forms that, ideally, have rounded corners but perfectly flat sides. A number of approaches to modelling facets in crystal growth are found in the literature:

<sup>1</sup> Or  $\gamma(\alpha\nabla\phi) = \alpha\gamma(\nabla\phi)$ .

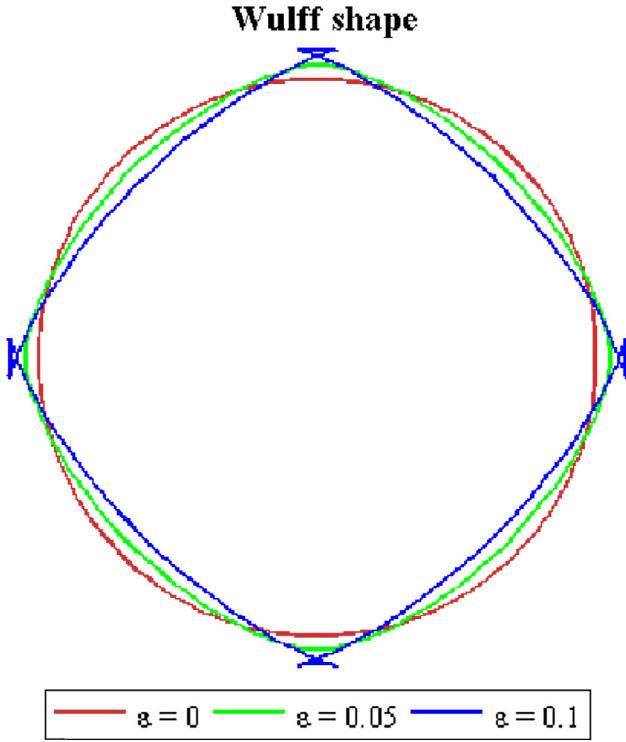


Fig. 3. The Wulff shape – see text for the construction.

1. In [7]

$$\begin{aligned}\eta &= 1 + \frac{2\epsilon|\phi_x\phi_y|}{\phi_x^2 + \phi_y^2} \\ &= 1 + 2\epsilon|\cos\theta\sin\theta| \\ &= 1 + \epsilon|\sin 2\theta|\end{aligned}\quad (8)$$

where [7] prefer to give the anisotropy in the form given in the first line.

2. In [8]

$$\eta = \begin{cases} 1 + \epsilon\cos(4\theta) & \theta_m \leq |\theta| \leq \pi/4 \\ \frac{\eta(\theta_m)\cos\theta}{\cos\theta_m} & |\theta| < \theta_m \end{cases}\quad (9)$$

This approach may be seen as regularising  $\eta = 1 + \epsilon\cos(4\theta)$  for  $\epsilon > 1/15$ .

3. In [9]  $\eta = 1 + \epsilon(|\sin\theta| + |\cos\theta|)$  is modified to remove cusps by

$$\eta = \begin{cases} 1 + \epsilon/\sin\theta_0 - \epsilon(\cot\theta_0 - 1)\cos\theta & \theta \leq \theta_0 \\ 1 + \epsilon(\sin\theta + \cos\theta) & \theta_0 < \theta < \pi/2 - \theta_0 \\ 1 + \epsilon/\sin\theta_0 - \epsilon(\cot\theta_0 - 1)\sin\theta & \theta \geq \pi/2 - \theta_0 \end{cases}\quad (10)$$

for  $0 \geq \theta \leq \pi/2$ , and by symmetry the other quadrants.

4. In [11] a kinetic anisotropy is given (we denote this by  $\eta_k$  to distinguish this from  $\eta$ ). Kinetic anisotropy appears in the mobility, not the free energy.

$$\eta_k = \begin{cases} 1 - \frac{\epsilon}{2} - \frac{\epsilon}{2}\cos[\pi(\theta - \pi/2)/\alpha] & |\theta - \pi/2| < \alpha \\ 1 & \text{otherwise} \end{cases}\quad (11)$$

5. In [12–14] the anisotropy is modelled both in both kinetic and surface energy form<sup>2</sup>

$$\eta_k = \left[ 1 + \left( \frac{1 - \cos(4\theta)}{2} \right)^\delta \right]^n \quad (12)$$

where [12] generalises the model (with values for  $\delta$  and  $n$  as 8 and 1 respectively) from [15] and use  $\delta = 64$  and  $n = 10$ . A less extreme illustration of this function is given in Fig. 4. This (kinetic anisotropy) is combined with a surface anisotropy  $(n_x^4 + n_y^4)^{1/4}$ , equivalent to  $3/4(1 + \epsilon\cos 4\theta)$ , with  $\epsilon = 1/3 > 1/15$ , and therefore has cusps. The combination appears in the reciprocal of mobility so we have here simply plotted its reciprocal, where we see its similarity with model 4.

6. In [10] two formulations are given, both kinetic anisotropy forms (with the surface energy left isotropic)

$$\eta_k^1 = 1 + \epsilon - 2\epsilon(1 - \cos 4\theta)^n/2^n \quad (13)$$

$$\eta_k^2 = 1 - \epsilon + 2\epsilon \tanh \frac{k}{|\tan 2\theta|} \quad (14)$$

Here  $n$  typically takes the values  $n < 10$  and  $1 < k < 2$ .  $\eta_k^1$  has smoother minimums than  $\eta_k^2$ .

A polar plot for each of these can be seen in Fig. 4. In models 4–6 anisotropy is included in the mobility,  $M$ , which we refer to as kinetic to distinguish it from surface energy modelling. However, as a sharp interface analysis shows, the velocity of the surface is both influenced by mobility and free energy construction, see [21]. A variant on the above approaches for the anisotropy function is found in [22], which gives  $\eta$  as a maximum of the dot product of the normal with the vector positions of the vertices. This function, though equivalent to a piecewise function of angle as, for example, in [11], has the merit of being easy to define for an arbitrary shape in any dimension.

It has been observed in [16] that having kinetic and surface anisotropy in proportion results in constant shape growth. The full possibilities for modelling include, then, both an anisotropic term in mobility and in free energy, which are not necessarily the same. Thus, there is a range of approaches to modelling faceted growth to choose from. We choose our approach to be closest to [9] and avoid a mobility anisotropy. This allows the equilibrium (and also low undercooling) shape to be the corresponding Wulff shape. We also adopt a regularised version of model 1 closer to [9] than [8] because we prefer to work with a model that allows control over the curvature at the vertices, leaving the facets flat. We also found that the extreme forms of anisotropy used in, for example, model 5, are problematic for the implicit computational mechanism we adopt [20]. Specifically, when the vertex radius can no longer be resolved by the mesh, instabilities arise. We do find though, with moderate anisotropic forms (that do not have ears), that similar behaviour is observed when the anisotropy function is included in the mobility (leaving the surface energy term isotropic) as when included in the surface free energy. Though a full exploration of combining each approach for a variety of undercoolings is left for future work.

There is another characteristic of the transition from the analytic domain to computational phase field: the argument of  $\gamma$  in the literature is  $\mathbf{n}$ , not  $\nabla\phi$ . In fact, the normal is not well defined away from the interface, and this problem is generally tackled in computer code rather than in the mathematical model. One way of dealing with this problem in the model is to define the normal

$$\mathbf{n} = \frac{\nabla\phi}{\nabla\phi \cdot \nabla\phi + q^2}, \quad (15)$$

for some small value,  $q$ .

The 6-fold anisotropy function we choose to work with, is a convenient variant of that found in [7], i.e.

<sup>2</sup> We present a corrected version here.

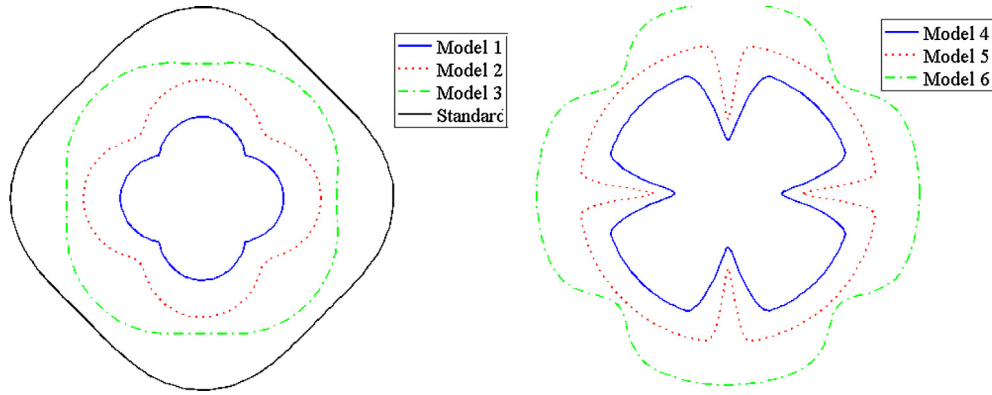


**Fig. 4.** Polar plots for models with 4-fold faceting in 2D found in the literature. On the left we also include the 4-fold continuous (non facet model) for comparison. On the right the kinetic based models 4–6. Note that in models 3 and 4 the orientation vary from the others by  $\pi/4$ .

$$\eta = 1 + \epsilon |\cos 3\theta|. \tag{16}$$

We adopt

$$\eta = \sqrt{1 + \epsilon |\cos 3\theta|}, \tag{17}$$

which simplifies the function  $A$ , appearing in the surface free energy:

$$\begin{aligned} A &= \frac{1}{2} \eta^2 \nabla \phi \cdot \nabla \phi \\ &= \frac{1}{2} (1 + \epsilon |\cos 3\theta|) \nabla \phi \cdot \nabla \phi. \end{aligned} \tag{18}$$

The model, Eq. (17) produces ears if  $\epsilon > 2/7$  (without the square root the limit is  $\epsilon = 1/8$ ). Intuitively Eq. (17) behaves in a similar way to Eq. (16) since, they are both zero degree homogeneous functions and, for small  $\epsilon$ , the two are essentially the same. In terms of components of  $\nabla \phi$  we find

$$\eta = \sqrt{1 + \epsilon \frac{|\phi_x^3 - 3\phi_x\phi_y^2|}{|\nabla \phi|^3}}. \tag{19}$$

We regularise this function using a single constant,  $q$ , which is less than the maximum value of  $|\nabla \phi|$ , as follows:

$$\eta = \sqrt{1 + \epsilon \sqrt{\frac{(\phi_x^3 - 3\phi_x\phi_y^2)^2 + q^6}{(\phi_x^2 + \phi_y^2 + q^2)^3}}}. \tag{20}$$

We find such a regularisation necessary for our code. This is because we employ an implicit solve at every time step, and as we let  $q \rightarrow 0$  the non-linearity of the derivatives of the modulus function increases and our code becomes unstable. It may well be that with other computational methods, e.g. weak form formulation or explicit solvers, such regularisation may be unnecessary. The parameter  $q$  regularises the function defined in Eq. (17) in a similar manner to that in models [8,9] but avoids dealing with piecewise functions or high exponents as in [12,10]. Unlike, the regularisation of [9], we see that it also allows a continuous interface stiffness,  $\eta(\theta) + \eta''(\theta)$ . The parameter,  $q < |\nabla \phi|_{\max}$ , is chosen to be sufficiently small to ensure that the resulting growth rates are independent of this parameter, but large enough to keep the simulation stable. Note that a choice of  $q > |\nabla \phi|$  begins to affect the results quantitatively. Adjusting  $\epsilon$  only affects the curvature at the vertices, where, again, we find that growth rates are not affected by this parameter even when the hexagon corners are visibly rounded. We illustrate the Frank shape in Fig. 5 for a variety of

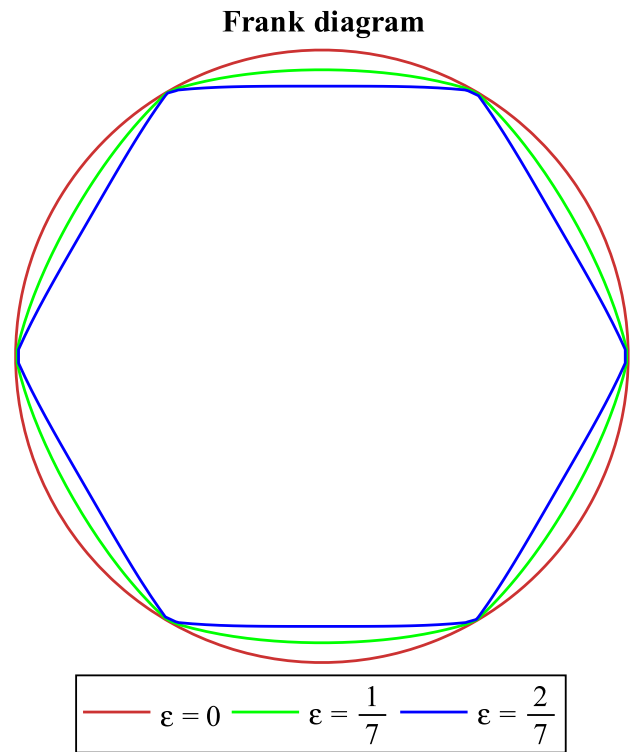


**Fig. 5.** Frank shape for  $\gamma = |\nabla \phi| \sqrt{1 + \epsilon |\cos 3\theta|}$ .

anisotropy strengths,  $\epsilon$ , and the resulting Wulff shape, with and without regularisation in Fig. 6 for anisotropy strength  $\epsilon = 0.133$ . To obtain the Wulff shape we obtain the locus

$$w(\theta) = \theta \rightarrow \left[ \frac{\partial \gamma}{\partial \phi_x}, \frac{\partial \gamma}{\partial \phi_y} \right]_{\phi_x = \frac{\cos \theta}{\delta}, \phi_y = \frac{\sin \theta}{\delta}} \tag{21}$$

where  $\delta \equiv 1/|\nabla \phi|_{\phi=0.5} = 4$ . A value of  $q = 0.2$  is almost indistinguishable from that of  $q = 0$ . Strictly speaking the theory of Wulff shapes only applies to these functions when  $q = 0$ , but it seems reasonable to expect such an expression to capture the salient properties when  $q > 0$ . It is illuminating to compare the interface stiffness,  $\xi = \eta(\theta) + \eta''(\theta)$ , for  $q = 0$  and the value used in our simulations,  $q = 0.2$ . This is achieved by writing

$$\eta(\theta) = \eta \left( \phi_x = \frac{\cos(\theta)}{\delta}, \phi_y = \frac{\sin(\theta)}{\delta} \right), \tag{22}$$

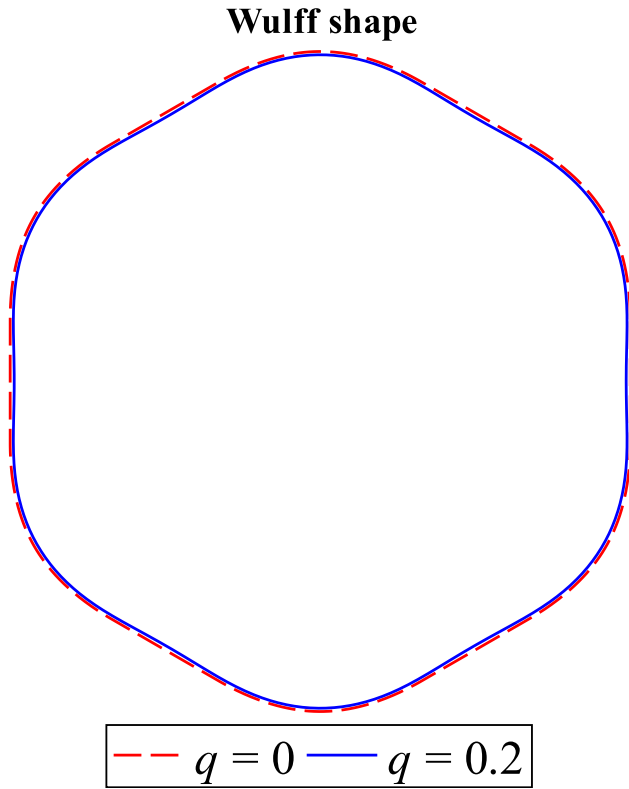


**Fig. 6.** Wulff shape for  $\gamma = |\nabla\phi| \sqrt{1 + \epsilon \sqrt{\frac{(\phi_x^2 - 3\phi_y^2)^2 + q^6}{(\phi_x^2 + \phi_y^2 + q^2)^3}}}$  for  $\epsilon = 0.133$ ,  $\delta = 4 = 1/|\nabla\phi|_{\phi=0.5}$ , with  $q = 0$  (dashed red) and  $q = 0.2$  (solid blue). The Wulff shapes are near indistinguishable, but with slight concavity in the sides for  $q = 0.2$ . (For interpretation of the references to color in this figure legend, the reader is referred to the web version of this article.)

where  $\delta = 4$  for our simulation. Note that, because of the presence of  $q$  the resulting curve is affected by the choice of  $\delta$ . A polar plot of interface stiffness,  $\xi = \eta + \eta''$ , is shown in Fig. 7, where the smoothing effect of the regularisation is clearly seen. For a fixed  $\epsilon, \delta$  one can explore the (maximum) size of  $\xi$  as a function of  $q$ . This

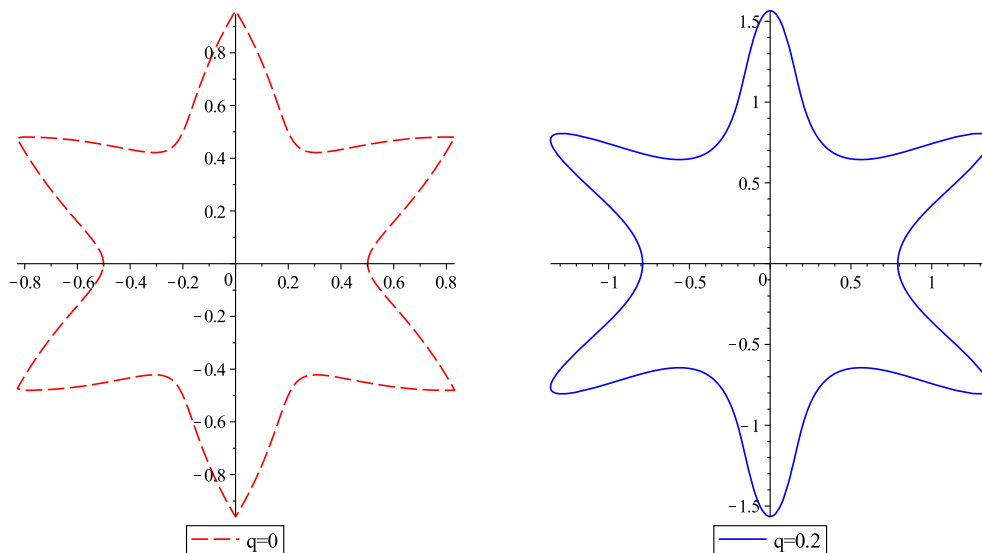


**Fig. 7.** Polar plots of Eq. (20) at  $|\nabla\phi|_{\phi=0.5} = 1/\delta = 0.25$  for both  $q = 0$  and  $q = 0.2$ . (red dashed, solid blue respectively). The parameter,  $q$ , can be seen to regularise the interfacial stiffness,  $\eta + \eta''$ , particularly at the outer extremes, e.g.  $\theta = \pi/6$ . (For interpretation of the references to color in this figure legend, the reader is referred to the web version of this article.)

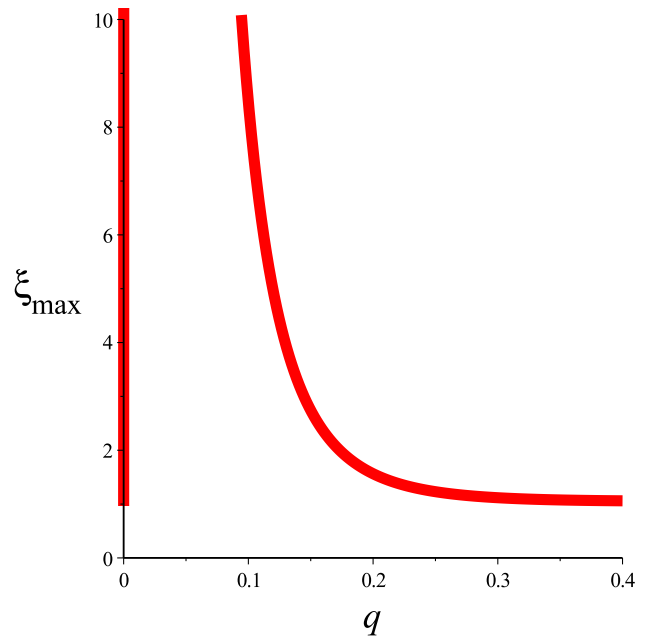


**Fig. 8.** The maximum value of the interface stiffness (at  $\theta = \pi/2$ ),  $\xi$ , as a function of  $q$  given  $\delta = 4, \epsilon = 0.133$ . For  $q = 0$  the maximum value is  $\xi_{\max} = 1$  but as  $q$  from zero,  $\xi_{\max}$  increases without bound. We choose  $q = 0.2$  for our simulations, which gives the interface stiffness illustrated in Fig. 7. Values of  $q$  which depart too much from  $q = 0.2$  lead to a  $\xi$  being substantially different from the  $q = 0$  case.

is seen in Fig. 8, which illustrates the effect of  $q$  on the size of interface stiffness,  $\xi_{\max}$ . For any value of  $q > 0, \eta'$  is continuous, but at  $q = 0$  there are values, for example,  $\theta = \pi/2$ , where  $\eta'$  is discontinuous, but has zero value either side of the discontinuity. This has the consequence that  $\eta''$  may be defined as zero at these points (and consequently  $\xi = 1$  here). Thus when  $\eta$  is regularised with  $q$ , very small values of  $q$  cause  $\xi$  to blow up without bound. Thus,  $q = 0.2$ , given  $\epsilon, \delta$ , is one of a narrow range of choices for  $q$  that returns an interface stiffness similar to that of the  $q = 0$  case (another option, for example, might be to choose  $q = 1/\delta = 0.25$  and tune  $\epsilon$  to  $\sim 0.4$ ). The general approach, then, is to choose an

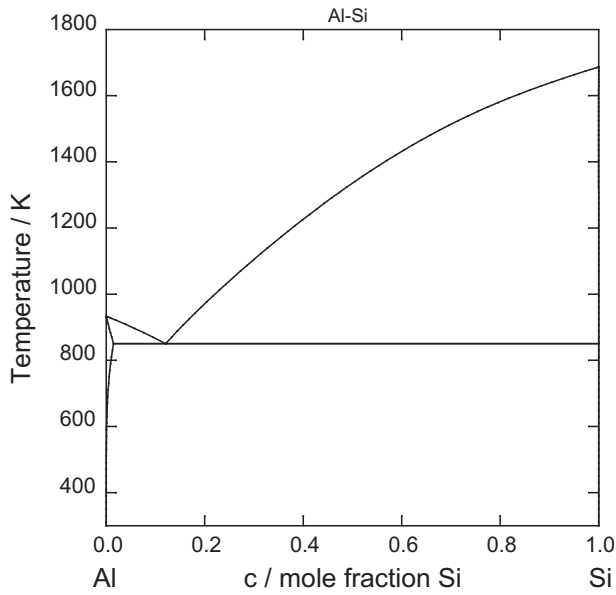


**Fig. 9.** Phase diagram for AlSi. For values of  $c > 0.5$  the mixed phase zone extends across a large temperature range. This allows the large undercooling essential for a dendritic structure to form from the faceted structure.

$\eta$  with  $q = 0$  that returns the desired Wulff shape and then, for a given interface width  $\delta$ , choose a  $q$  which gives a smoother  $\zeta$ , but otherwise qualitatively similar in size and shape.

### 3. The phase field model

The equations for phase and concentration are given by:

$$\dot{\phi} = -M \frac{\delta F}{\delta \phi}, \quad (23)$$

and

$$\dot{c} = -\nabla \cdot D \nabla \frac{\delta F}{\delta c} \quad (24)$$

where  $M$  and  $D$  are the mobility and solute diffusion parameters respectively, and defined as follows:

$$M = M^{\text{Al}}(1 - c) + M^{\text{Si}}c, \quad (25)$$

where  $M^{\text{Al}}$ ,  $M^{\text{Si}}$  are the mobilities of each component separately, and

$$D = \frac{D^{\text{liq}}\phi + D^{\text{sol}}(1 - \phi)}{RT} c(1 - c), \quad (26)$$

where the diffusivity in the solid,  $D^{\text{sol}} \ll D^{\text{liq}}$ . The temperature is given by  $T$ . The free energy  $F$ , is given in terms of free energy density,  $f$ ,

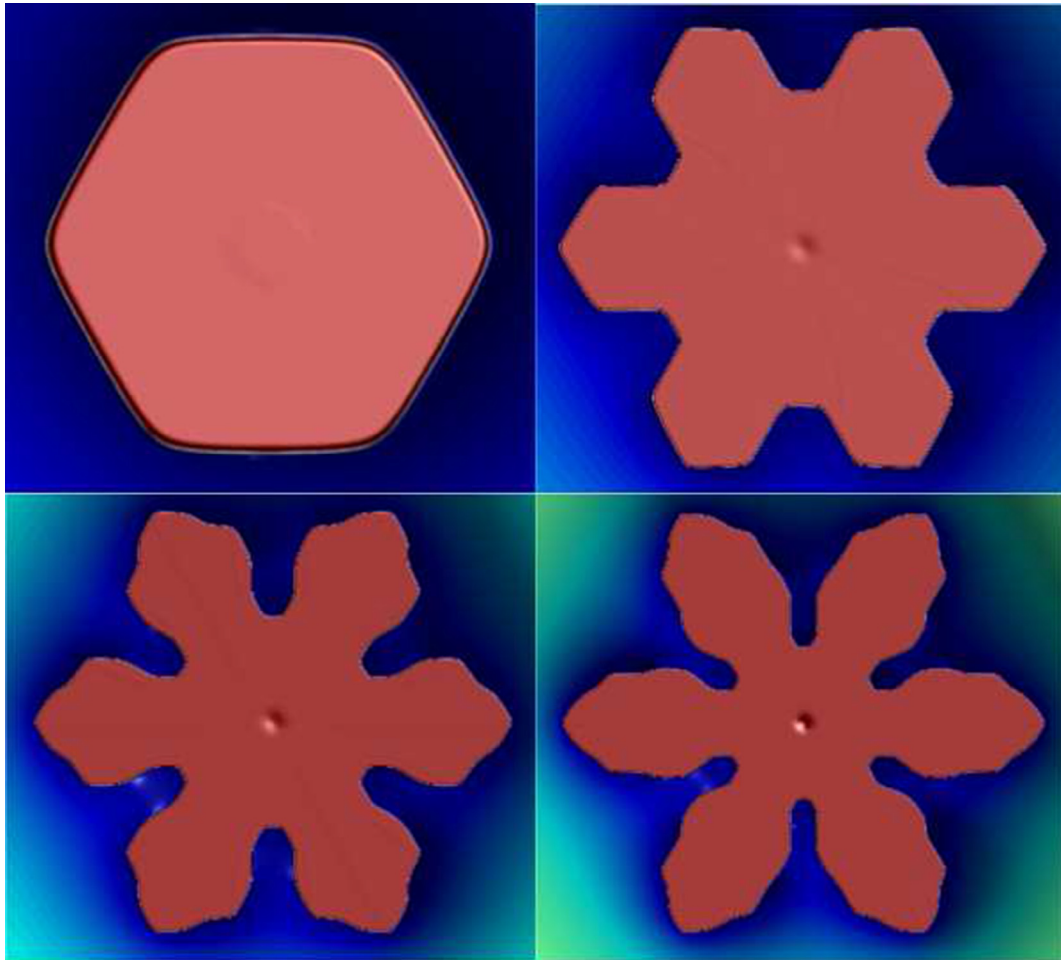


**Fig. 10.** Clockwise from top left, the morphology for  $T = 1300$  K,  $T = 1200$  K,  $T = 1000$  K and (bottom left)  $T = 1100$  K. Each plot is a function of solute concentration, the solid being effectively pure Silicon ( $c = 1$ ) with the Aluminium still in liquid form. The blue area around the crystal indicates the depletion of Silicon close to the growing edge  $c \sim 0.3$  Si. For  $T = 1000$  K. (For interpretation of the references to color in this figure legend, the reader is referred to the web version of this article.)

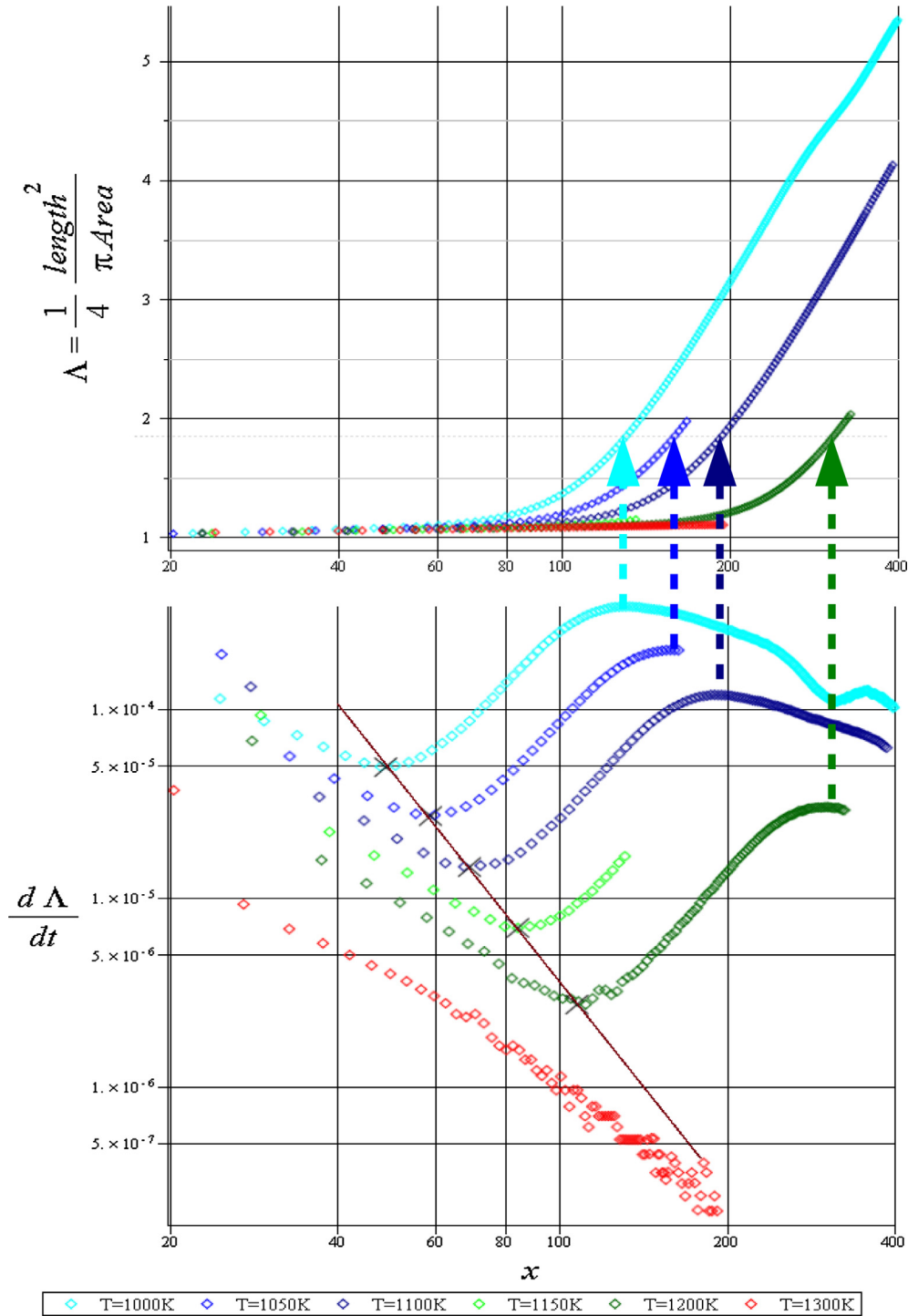


**Fig. 11.** The top figure shows the evolution of  $\Lambda$  as a function of vertex position,  $x$ , for a range of temperatures,  $T$ . The lower figure (on a log-log scale) shows the evolution of  $d\Lambda/dt$ , revealing a series of minima and maxima (please see text for further observations).

$$F = \int_{\Omega} f d^3x. \quad (27)$$

The two key components of  $f$  are the surface free energy density and the bulk free energy:  $f = f_s + f_B$ . The bulk free energy density is built in terms of the bulk free energies of the separate components for each phase

$$f_B = g(\phi)f_{\text{liq}}(c, T) + (1 - g(\phi))f_{\text{sol}}(c, T), \quad (28)$$

Here we use the interpolating function  $g(\phi) = \phi^2(3 - 2\phi)$ . The quantities  $f_{\text{liq}}(c, T)$  and  $f_{\text{sol}}(c, T)$  may be found, for example, in [23]. See Fig. 9 for an equilibrium phase diagram for AlSi. This material allows significant undercooling in the mixed phase region, e.g.  $c = X_{\text{Si}} = 0.6$ , has a temperature range of  $\Delta T > 400$  K. The surface energy density contains terms to control the interface width and, in particular, the anisotropy, discussed in the previous section.

$$f_S = W[A(\nabla\phi) + B(\phi)]. \quad (29)$$

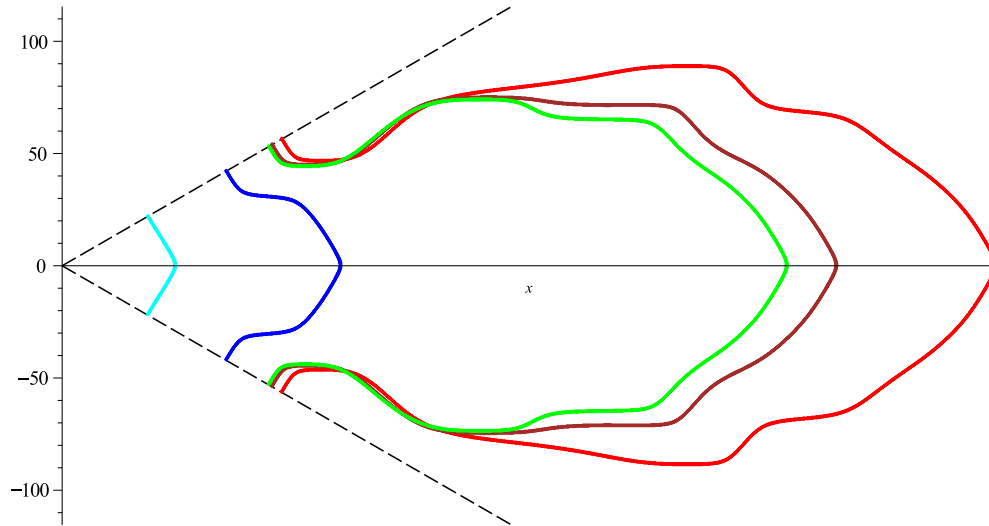


**Fig. 12.** The morphology change in position (and time) at the lowest temperature simulated,  $T = 1000$  K. The crystal shapes are shown on a one sixth domain and each snapshot is taken near the key points,  $d\Lambda/dt$ , with the exception of the red curve which is simply the final snapshot. (For interpretation of the references to color in this figure legend, the reader is referred to the web version of this article.)

Here  $W = W^{Al}(1 - c) + W^{Si}c$ , is a linear combination of the alloy components,  $B = 8\phi^2(1 - \phi)^2$  is a double well potential used to control the interface width, and  $A$ , controls the interface width and anisotropy. The isotropic case is given by  $A = \frac{1}{2}\delta^2\nabla\phi \cdot \nabla\phi$ . A 1D solution to  $\frac{\delta F_s}{\delta\phi} = 0$

$$\phi = \frac{1}{2} \left[ 1 + \tanh \left( \frac{2x}{\delta} \right) \right]. \quad (30)$$

defines the interface width, where note that we implicitly adopt  $\delta = 1/|\nabla\phi|$ .

#### 4. Results

In order to discuss and interpret the simulation results we introduce a dimensionless measure of faceting,  $\Lambda$ . The measure is invariant under scaling and is normalised so that a circle returns a value of unity. Any other closed shape will have a value  $\Lambda > 1$ . We define

$$\Lambda = \frac{\text{Perimeter}^2}{4\pi \times \text{Area}} \quad (31)$$

We also find that the quantity  $d\Lambda/dt$  is very sensitive to changing morphology in the growth in time. Broadly speaking,  $d\Lambda/dt \approx 0$  indicates a self similar expanding shape. A regular hexagon has

$$\Lambda = \frac{36}{4\pi 3\sqrt{3}/2} \approx 1.10 \quad (32)$$

and a square  $\Lambda \approx 1.27$ , etc. We find, in agreement with [1] that small undercooling produces a growing self similar (in this case hexagonal) facet, but for large undercoolings we see facet *breaking* and ultimately dendritic structures. For the latter case we broadly expect the value of  $\Lambda$  to increase from unity (the initial condition of a circular seed) in time, perhaps monotonically. In fact we also find that in the early stages a regular hexagon develops for all undercooling considered. Thus, we are not just interested in the change in morphology, between different undercoolings, but also within the growth cycle of each single undercooling.

Fig. 10 shows the evolution of crystal shape as a function of temperature, chosen at the same position (apart from  $T = 1300$  K which had not attained that size). Fig. 11 shows plots of  $\Lambda$  (top)

and  $\dot{\Lambda} \equiv d\Lambda/dt$  against vertex position,  $x$ , for a range of temperatures,  $T = 1000$  K, 1050 K, 1100 K, 1150 K, 1200 K, 1300 K. Following  $\Lambda$  for the largest undercooling, at  $T = 1000$  K, we see that  $\Lambda$  is largest for this, lower, temperature, and also exhibits a series of minima and maxima. A large value of  $\Lambda$  indicates the largest departure from a circle/hexagon, and thus a large positive value for  $\ddot{\Lambda}$  (and  $\frac{\partial}{\partial x}\dot{\Lambda}$ ) at the first minimum ( $\dot{\Lambda} = 0$ ) indicates facet breaking. Thus an insight into the relation between facet breaking and temperature is found by finding the trend between the occurrence of this first minimum for each temperature. This forms a trend shown by the brown solid straight line passing through these first minima (indicating a power law between the facet breaking position and temperature). With larger temperature the minima become shallower and by  $T = 1300$  K appear to disappear and thus, for this temperature (and for  $1300 \text{ K} < T < T_M$ ), is predicted to remain hexagonal. The other observation in Fig. 11 is that the position of the first minima  $d\Lambda/dt$  are all near hexagonal and the position of the first maxima for each undercooling have the same morphology (loosely described as a faceted hexagonal star shape – see top right in Fig. 10). This correlation between different undercooling is shown by the vertical dashed arrow lines joining the upper and lower figures at the first maxima for a selection of four undercoolings (the first minima also coincide with a value of  $\Lambda \sim 1.1$  indicating a faceted hexagon). Fig. 12 illustrates the changes in morphology for a single undercooling ( $T = 1000$  K). All the shapes, at different undercooling, in Fig. 10 are present also within different stages of the single simulation  $T = 1000$  K. In Fig. 12 the stages chosen are the minima and maxima points of  $d\Lambda/dt$  plus the final shape attained in the simulation at the end (i.e. minimum, maximum, minimum, maximum, final shape, respectively). Clearly, following the first minimum the rapid change of morphology is due to the formation of the six arms along the vertices. Following the second minimum the rapid change is due to the flattening out of the sides of dendrite (compare green with brown). Finally, we consider the relationship between facet length and velocity. Specifically: what is the relation between maximum length of the hexagonal side and velocity just before breaking? By looking at Fig. 11 we can extract the breaking positions, and therefore facet length,  $L = x$ , the tip position at the minima. Using tip speed,  $V$ , at this point and linear regression we found the power law relation for this data.

$$L \propto V^{-0.54} \approx \frac{1}{\sqrt{V}} \quad (33)$$

Qualitatively larger facets are produced with lower growing speeds according to this rule for all temperatures we studied below  $T = 1300$  K.

### Acknowledgements

This research was funded by EPSRC Innovative Manufacturing Research Hub in Liquid Metal Engineering (LiME), Grant No. EP/N007638/1.

We would like to thank the reviewers for their observations and suggestions for this paper.

### References

- [1] R.B. Liu, D.M. Herlach, M. Vandyoussefi, A.L. Greer, Morphologies of silicon crystals solidified on a chill plate, *Met. Mater. Trans. A* 35A (2003) 1067–1073.
- [2] C. Panofen, D.M. Herlach, Solidification of highly undercooled Si and Si-Ge melts, *Met. Mater. Trans. A* 449A (2007) 699–703.
- [3] X.B. Yang, K. Fujiwara, K. Maeda, J. Nozawa, H. Koizumi, S. Uda, Dependence of Si faceted dendrite growth velocity on undercooling, *Appl. Phys. Lett.* 98 (2011) 012113.
- [4] S.E. Battersby, R.F. Cochrane, A.M. Mullis, Highly undercooled germanium: growth velocity measurements and microstructural analysis, *Mater. Sci. Eng. A* 226 (1997) 443–447.
- [5] S.E. Battersby, R.F. Cochrane, A.M. Mullis, Growth velocity-undercooling relationships and microstructural evolution in undercooled Ge and dilute Ge-Fe alloys, *J. Mater. Sci.* 34 (1999) 2049–2056.
- [6] J.W. Xian, S.A. Belyakov, K. Nogita, H. Yasuda, C.M. Gourlay, Faceted and nonfaceted growth of  $\text{Cu}_6\text{Sn}_5$  crystals, *Proc. Int. Conf. Sol. Proc.* (2017) 251–254.
- [7] J.E. Taylor, J.W. Cahn, Diffuse interfaces with sharp corners and facets: phase field models with strongly anisotropic surfaces, *Physica D* 112 (1998) 381–411.
- [8] J.J. Eggleston, G.B. McFadden, P.W. Voorhees, *Physica D* 150 (2001) 91–103.
- [9] J.-M. Debierre, A. Karma, F. Celestini, R. Guerin, Phase-field approach for faceted solidification, *Phys. Rev. E* 68 (2003) 041604.
- [10] T. Uehara, R.F. Sekerka, Phase field simulations of faceted growth for strong anisotropy of kinetic coefficient, *J. Cryst. Growth* 254 (2003) 251–261.
- [11] H. Miura, Anisotropy function of kinetic coefficient for phase-field simulations: reproduction of kinetic Wulff shape with arbitrary face angles, *J. Cryst. Growth* 367 (2013) 8–17.
- [12] H.K. Lin, H.Y. Chen, C.W. Lan, Adaptive phase field modelling of morphology instability and facet formation during direction solidification of SiGe alloys, *J. Cryst. Growth* 385 (2014) 44–48.
- [13] H.K. Lin, H.Y. Chen, C.W. Lan, Phase field modelling of facet formation during directional solidification of silicon film, *J. Cryst. Growth* 385 (2014) 134–139.
- [14] H.K. Lin, C.W. Lan, Three-dimensional phase field modeling of silicon thin-film growth during directional solidification: facet formation and grain competition, *J. Cryst. Growth* 401 (2014) 740–747.
- [15] W. Miller, N. Abrosimov, I. Rasin, D. Borrisova, *J. Cryst. Growth* (2008) 310.
- [16] E. Yokoyama, R.F. Sekerka, A numerical study of the combined effect of anisotropic surface tension and interface kinetics on pattern formation during the growth of two-dimensional crystals, *J. Cryst. Growth* 125 (1992) 389–403.
- [17] R.F. Sekerka, Equilibrium and growth shapes of crystals: How do they differ and why should we care?, *Cryst Res. Technol.* 40-4/5 (2005) 291–306.
- [18] M. Salvalaglio, R. Backofen, Faceting of equilibrium and metastable nanostructures: a phase-field model of surface diffusion tackling realistic shapes, *Cryst. Growth Des.* 15 (2015) 2787–2794.
- [19] K. Wang, M. Wei, L. Zhang, Y. Du, Morphologies of primary silicon in hypereutectic Al-Si alloys: phase field simulation supported by key experiments, *Metall. Mater. Trans. A* 47A (2016) 1510–1516.
- [20] P.C. Bollada, C.E. Goodyer, P.K. Jimack, A.M. Mullis, F.W. Yang, Three dimensional thermal-solute phase field simulation of binary alloy solidification, *J. Comput. Phys.* 287 (2015) 130–150.
- [21] G.B. McFadden, A.A. Wheeler, R.J. Braun, S.R. Coriell, Phase-field models for anisotropic interfaces, *Phys. Rev. E* 48 (3) (1993) 2016–2024.
- [22] F. Wendler, C. Mennerich, B. Nestler, A phase-field model for polycrystalline thin film growth, *J. Cryst. Growth* 327 (2011) 189–201.
- [23] J. Groebner, H.L. Lukas, F. Aldinger, *CALPHAD* 20 (1996) 2247–2254.